

# g4chargeit: Geant4-based kinetic Monte Carlo simulations of charging in dielectric materials

Kush P. Gandhi<sup>a</sup>, Advik D. Vira<sup>a</sup>, William M. Farrell<sup>b</sup>, Nikolai Simonov<sup>a</sup>, Alvaro Romero-Calvo<sup>c</sup>, Thomas M. Orlando<sup>a,d</sup>, Phillip N. First<sup>a</sup>, Zhigang Jiang<sup>a</sup>

<sup>a</sup>*School of Physics, Georgia Institute of Technology, Atlanta, GA, USA*

<sup>b</sup>*NASA Goddard Space Flight Center, Greenbelt, MD, USA*

<sup>c</sup>*Daniel Guggenheim School of Aerospace Engineering, Georgia Institute of Technology, Atlanta, GA, USA*

<sup>d</sup>*School of Chemistry and Biochemistry, Georgia Institute of Technology, Atlanta, GA, USA*

---

## Abstract

We present g4chargeit, a kinetic Monte Carlo framework built on Geant4 for self-consistent simulation of time-dependent electrostatic charging in dielectric materials. The model explicitly incorporates stochastic particle transport and scattering processes using validated Geant4 cross-sections, while self-consistently evolving the electric potential and field. As a representative application, we simulate the charging of regolith grains under average dayside conditions on the Moon. The surface of the Moon, in addition to other airless planetary bodies, are regularly exposed to solar ultraviolet photons and solar-wind plasma, creating a radiation environment in which electrostatic interactions among regolith grains become significant. Until now, simulations of regolith charging have often relied on analytical approximations that oversimplify grain geometry and interaction mechanisms. Our Geant4-based simulations reveal charge accumulation within intergrain micro-cavities, leading to repulsive electrostatic forces consistent with experimental observations. The framework establishes a multiscale approach that links microscopic scattering events to the continuity equation of surface charge density and to the formation of macroscopic surface charge patches in complex grain geometries. Although demonstrated here for planetary regolith, the method is general and applicable to a broad range of dielectric charging problems. The code is openly available at <https://github.com/kgandhi63/g4chargeit.git>.

**Keywords:** Geant4, Kinetic Monte Carlo, Multiscale simulations, Electrostatic field evolution, Grain-scale charging, Micro-cavities

---

## 1. Introduction

Kinetic Monte Carlo (KMC) simulations of dielectric materials are of broad interest across multiple fields, including the modeling of photovoltaic devices [1], electrostatic forces in DNA packing [2, 3], radiation transport in semiconductors [4, 5], and dielectric breakdown in space equipment [6, 7]. Radiation transport is commonly simulated using Monte Carlo (MC) codes because of their generalizability and computational efficiency, employing random walks to sample complex transport dynamics. However, such MC codes often lack the capability to self-consistently model time-evolving phenomena, such as charge accumulation [5, 8]. As a result, these simulations frequently require multiple interdependent simulation toolkits, leading to hybridized computational models [6, 7, 9, 10].

A sought-after application of KMC simulations is modeling the charge evolution of regolith dust on airless bodies, which is critical both for advancing our understanding of fundamental planetary surface processes and for addressing practical challenges in space exploration [11]. Airless bodies possess virtually no atmosphere and are therefore exposed to solar ultraviolet (UV) radiation, which produces photoelectrons (PEs), as well as to solar-wind (SW) plasma. For example, regolith grains on the Moon’s surface become electrically charged [12, 13, 14]. The behavior of these charged grains influences several key processes, including modification of the local plasma environment, which affects dust transport and adhesion and, in turn, impacts the performance and longevity of equipment such as solar panels, spacesuits, and optical instruments [15, 16, 17, 18]. Regolith-grain mobility also has important implications for in situ resource utilization, instrument degradation, and habitat contamination. The charging of regolith grains further affects the performance of electrodynamic dust shields and filtration devices, and electrostatic adhesion to lunar exploration systems [19, 20].

The accumulation of charge is primarily driven by the reabsorption of emitted PEs, especially within micro-cavities formed between neighboring regolith grains, leading to heterogeneous and spatially patchy charge distributions. This localized charge buildup can trigger dust lofting or even dielectric breakdown [21, 22, 23, 24, 25]. To quantify these effects, Wang et al. [24] introduced the patched-charge model, which emphasizes the role of micro-cavities in facilitating localized charge accumulation on airless planetary bodies such as the Moon. The patched-charge model considers a portion of a grain within the regolith bed that emits PEs and/or secondary electrons into a cavity, resulting in repulsive forces between surrounding grains [24]. Complementary to this work, Zimmerman et al. [26] developed a purely analytical model for charge buildup on hexagonally packed spherical grains and showed that electric fields can reach strengths of MV/m in less than one lunar day—sufficient to induce dielectric breakdown [26]. However, these analytical models neglect the effects of non-spherical and asymmetrical grain geometries and lack the capability to explore dependencies on grain composition.

In this article, we model charge accumulation within micro-cavities of regolith grains on airless bodies to demonstrate the capabilities of our KMC framework built in Geant4 (GEometry AND Tracking) [27, 28, 29]. By leveraging the capabilities of Geant4, we enable simulations with arbitrary geometries and material compositions while capturing the stochastic nature of electron emission, reabsorption, and SW interactions on a grain-by-grain basis and evolving the resulting electric field in situ. We employ a self-consistent MC architecture that links microscopic scattering events to the continuity equation of surface charge density, enabling accurate simulation of regolith grain charging dynamics. We benchmark our Geant4-based code, called `g4chargeit`, against a simple stacking of spheres [26] and the patched-charge model [24]. This work provides an open-source, all-in-one software package for the broader scientific community.

The remainder of the paper is organized as follows. Section 2 describes the simulation framework, and Section 3 details the implementation and execution. Section 4 presents grain stacking configurations of increasing complexity and demonstrates the capabilities of the code. The paper concludes with a discussion of limitations and potential applications beyond space science.

## 2. Simulation Framework

Geant4 is an open-source, C++-based simulation toolkit used to model particle scattering and transport through matter, with applications in high-energy, nuclear, medical, and space physics [27, 28, 29]. Our MC framework for time-dependent simulations of electrostatic fields is built in Geant4 (version 11.3.0). The following extensions to Geant4 are incorporated into `g4chargeit`:

(i) Geometry Description Markup Language (GDML) for importing complex geometries and computer-aided design (CAD)-based structures [30], (ii) Open Multi-Processing (OpenMP) for parallelizing the simulations [31], (iii) ROOT for data storage and post-simulation analysis [32], (iv) General Particle Source (GPS) for defining isotropic or anisotropic radiation sources, and (v) g4pbc for implementing periodic boundary conditions (PBCs). Building on these extensions, g4chargeit includes a custom class, `AdaptiveSumRadialFieldMap.cc`, which adaptively computes the electric field from local charges determined in the previous MC simulation iterations, as described below.

### 2.1. Iterative Approach for Time-Evolved Electric Field

The Geant4 toolkit is typically limited by the fact that it does not explicitly model electrodynamics. As a result, particle interactions with the material and electric field are not inherently self-consistent, preventing individual time-steps and trajectories from influencing one another. To circumvent this limitation, we re-initialize the MC simulation at each discretized time step to include the electric-field contributions of charged particles from earlier steps. Specifically, an initial Geant4 simulation is performed for the zeroth iteration ( $n = 0$ ), in which particle transport is modeled based on the probabilistic nature of ionization and scattering processes inside the grains (Appendix A). Then, for each subsequent iteration, the simulation is re-initialized with the deposited charges of the previous iterations, such that the pre-existing electric field influences subsequent particle trajectories.

Figure 1 provides an overview of our dynamical, self-consistent simulation framework. The custom class `AdaptiveSumRadialFieldMap.cc` calculates the electric field by superimposing the point-charge contributions from  $N$  charges embedded within the grains from prior iterations, using adaptively binned octrees (described in Section 2.1.1). For the  $i$ -th embedded particle with charge  $q_i$  at position  $\mathbf{r}_i$ , the electric potential contribution is

$$\varphi_i(\mathbf{r}) = \frac{1}{4\pi\epsilon_r\epsilon_0} \frac{q_i}{|\mathbf{r} - \mathbf{r}_i|}, \quad (1)$$

where  $i \in \mathbb{Z} : [1, N]$ ,  $\epsilon_r$  is the dielectric constant, and  $\epsilon_0$  is the vacuum permittivity. At the end of the  $n$ -th iteration, the locations of all newly deposited charges are recorded and appended to a master list containing the charge-distribution history from iteration  $n - 1$ . With each successive iteration, this master list is loaded, and the total electric field  $\mathbf{E}(\mathbf{r})$  is recalculated by superimposing the contributions of all charges in the geometry, providing a self-consistent model of charge accumulation and the resulting changes in the local electric field. Charge dissipation is also applied for each iteration based on the conductivity and dielectric constant of the material (Appendix B).

#### 2.1.1. Adaptive Meshing of Electric Field

A direct summation of deposited charges is computationally infeasible for simulations involving millions of particles. This limitation precludes the use of conventional approaches based on solving Laplace's equation with boundary potentials or Poisson's equation with charge-density distributions, both of which still require repeated iteration over all deposited charges. To address this intractability, we implement two adaptive octrees: one for electric-field calculation,  $O_{\text{field}}$ , and the other for storing surface charges,  $O_{\text{charge}}$  [33]. An illustration of the initial construction of these two octrees is shown in Fig. 1 (top region, dashed box).

$O_{\text{charge}}$  is initially constructed by assigning deposited charges to voxels, which are subregions of  $O_{\text{charge}}$  generated within the geometry. These voxels are then dynamically split until either a

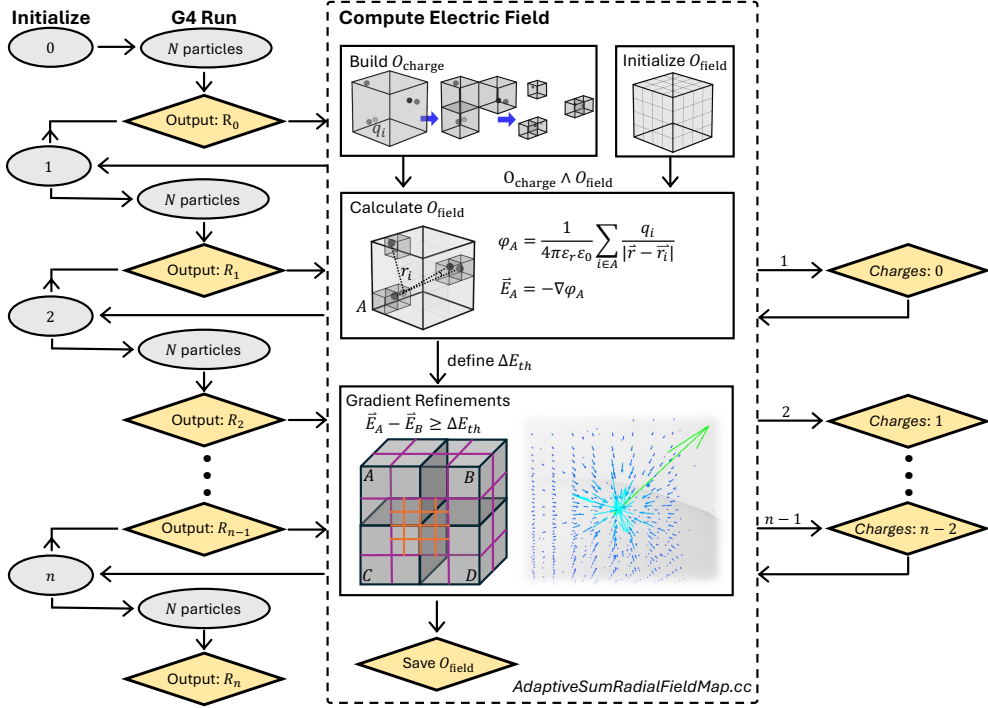


Figure 1: Self-consistent simulation framework of *g4chargeit*.  $N$  particles are sampled and transported through the geometry for the  $n$ -th iteration. The particle trajectories are saved in the ROOT file (denoted as  $R_i$ ), and deposited charges are aggregated into a master charge list (denoted as *Charges*), which is used to compute the electric field. The custom *AdaptiveSumRadialFieldMap.cc* class (dashed box) is structured as follows: a charge octree,  $O_{\text{charge}}$ , is constructed, followed by a field octree,  $O_{\text{field}}$ , generated using a Barnes–Hut approximation to efficiently evaluate the electric field (resulting in a scalar potential  $\varphi_A$  with a corresponding field  $\vec{E}_A$  for a specific octree voxel  $A$ ). The field octree is adaptively binned if the field gradient between neighboring cells exceeds the threshold  $\Delta E_{\text{th}}$ . An example of the refined  $O_{\text{field}}$  is shown as an inset, where the density of the pre-computed electric-field vectors (arrows) scales as the field approaches the deposited charge (center of the image). The dynamical process is repeated for  $n$  iterations by self-consistently updating the charge distributions and field maps.

single integer charge remains or the user-specified minimum voxel size is reached. After  $O_{\text{charge}}$  is mapped,  $O_{\text{field}}$  is created with a uniform coarse grid with a user-defined depth that sets the initial voxel size.  $O_{\text{field}}$  is populated using the charges placed in  $O_{\text{charge}}$ , as illustrated in Fig. 1. A Barnes–Hut algorithm is implemented to approximate distant charge clusters as point multipole moments, thereby reducing the computational load [34]. The final result is an efficiently optimized electric-field map.

To further reduce the computational load, the framework recursively evaluates the electric-field gradient across the grid; cells exhibiting gradients above a specified threshold are adaptively refined. This adaptive refinement generates a non-uniform mesh within  $O_{\text{field}}$  that concentrates computational resolution in regions of large field gradients, such as the micro-cavities between grains. An example of the adaptively meshed electric field is shown in Fig. 1 (inset, gradient refinements box), where the density of electric field computations is concentrated around the embedded charge. Although the discretized electric field formally contains singularities at the

locations of individual embedded charges, the local electric potential away from each charge varies smoothly, scaling as  $1/r$ . When the field is appropriately binned, these singular features are removed, resulting in a smooth effective charge distribution. In certain cases, a bin in the field octree may contain  $N_v$  materials with varying degrees of conductivity. To account for material variation within a single bin, a weight  $w_i$ , corresponding to the volume occupation fraction, is assigned to each dielectric constant  $\varepsilon_i$ . The effective dielectric constant of the bin is then given by

$$\varepsilon_r^{-1} = \sum_{i=1}^{N_v} w_i \varepsilon_i^{-1}. \quad (2)$$

Consequently, both the microscopic and macroscopic electric potentials and fields remain continuous and free of nonphysical discontinuities, while accurately reflecting the electromagnetic properties. [35].

The final electric-field map is called back into the MC framework, overriding the Geant4-defined field class. Particle trajectories in the resulting electric-field topology are integrated using `G4DormandPrince745`, a Geant4 field solver that employs a high-order adaptive Runge–Kutta stepper based on the efficient Dormand–Prince (DoPri5) method. The integration accuracy is controlled via the `DeltaOneStep` parameter set within the `DetectorConstruction` class; in our simulations, this parameter is set to  $0.1 \mu\text{m}$ , ensuring precise tracking of particle motion [36].

## 2.2. Probabilistic Scattering and Interaction Physics

Geant4 enables explicit simulation of individual ionization and scattering interactions, providing a versatile toolkit for modeling the production and subsequent propagation of secondary particles. This approach differs from conventional particle-in-cell methods, which typically rely on assumptions regarding secondary particle yields [26]. The cross-section models and databases used in our Geant4 simulations are described in Appendix A. Here, we demonstrate the particle-tracking capabilities by considering species relevant to the space environment: low-energy solar photons, as well as monoenergetic protons and low-energy electrons from the SW plasma [12]. For simplicity, we consider hexagonally packed spheres, each with a radius of  $100 \mu\text{m}$  and composed of  $\text{SiO}_2$ . Figure 2 shows a cross-sectional view of particle interactions with the  $\text{SiO}_2$  spheres (with  $\varepsilon_r = 3.9$ ) and the adaptively computed electric field for 39 prior iterations in Fig. 2a and 17 prior iterations in Fig. 2b,c (refer to Section 4.2 for details on particle fluxes).

*Photoelectron Trajectories.* Approximately 85% of the photons, sampled from the solar spectrum with an incident angle of  $45^\circ$  (Fig. 3d), undergo the photoelectric effect in our  $\text{SiO}_2$  spheres. Of these events, three dominant outcomes are observed with the following probabilities: (1) PE stops near the surface of the sphere (occurring  $\sim 97\%$ ), (2) PE scatters out of its originating volume and strikes a neighboring sphere (occurring  $\sim 2\%$ ), or (3) PE backscatters and escapes the simulation volume (occurring  $\sim 1\%$ ). An example of each scenario is depicted in Fig. 2a. The photon labeled 1 in Fig. 2a has an initial energy of 233 eV and travels 334 nm before undergoing the photoelectric effect. The resulting PE, with an energy of 129 eV, travels 0.5 nm before stopping near the surface of the sphere. In this event, an Auger electron with an energy of 87 eV is also emitted and stops within 0.8 nm of the initial photoemission site. In contrast, the photon labeled 2 has an initial energy of 68 eV and interacts within 1.5 nm of the  $\text{SiO}_2$  surface, producing a PE with an energy of 55 eV. This PE traverses 3.6 nm of  $\text{SiO}_2$  and exits its originating volume with an energy of only 0.6 eV. Due to the strong electric fields within the cavity between spheres,

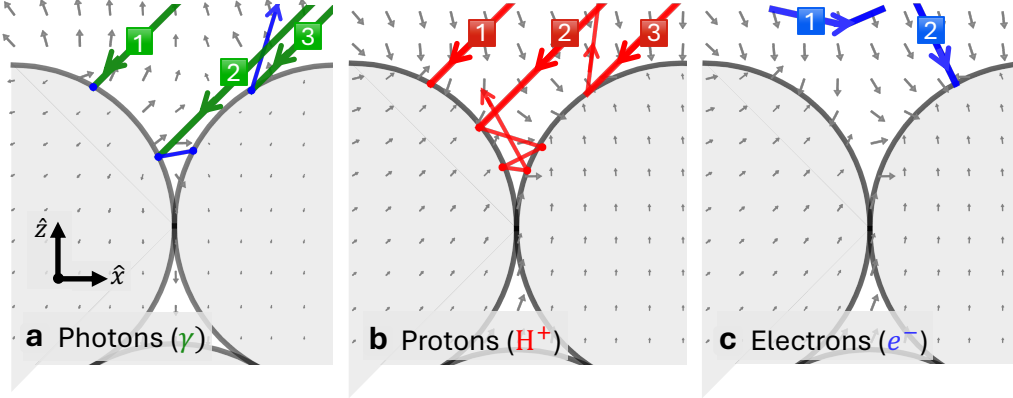


Figure 2: Cross-section of hexagonally packed grains (with radius of  $100\mu\text{m}$ ) overlaid with the electric-field map (gray arrows, scaled by field magnitude) in the  $xz$ -plane. Representative particle trajectories are shown for (a) photons undergoing a PE event, (b) 1 keV protons, and (c) low-energy electrons (isotropic in angle). The electric-field maps for photons (a) and SW (b,c) are shown at iterations  $n = 39$  and  $n = 17$ , respectively, with a dielectric constant of  $\epsilon_r = 3.9$ .

the PE subsequently loses an additional 0.4 eV before entering a neighboring sphere (blue trajectory in Fig. 2a), where it stops within 0.4 nm. Finally, a 41 eV photon, labeled 3 in Fig. 2a, undergoes the photoelectric effect within 0.4 nm upon interacting with the sphere, producing a 27 eV PE that backscatters and escapes the sphere.

*Proton Trajectories.* The 1 keV protons from the SW plasma, incident at an angle of  $45^\circ$ , undergo Columbic scattering in  $\text{SiO}_2$  and typically implant within  $\sim 18\text{ nm}$  (e.g., proton trajectory labeled as 1 in Fig. 2b). This implantation depth is consistent with results from other simulation codes and experimental results (implantation depth of  $\sim 22 \pm 13\text{ nm}$  reported in Ref. [37]). The proton labeled 2 in Fig. 2b interacts with one sphere, losing 660 eV before scattering out and bouncing between the spheres until it escapes the cavity with an energy of 244 eV after traveling a total distance of 16 nm in both spheres. The third proton shown in Fig. 2b gains 1 eV while interacting with the strong electric fields near the highly illuminated faces of the spheres, then deposits 950 eV over 14 nm before backscattering out of the sphere and exiting the simulation volume.

*Electron Trajectories.* Thermal electrons ( $< 80\text{ eV}$ ), incident isotropically in angle, are introduced simultaneously with the 1 keV protons to model the SW plasma. The electron labeled 1 in Fig. 2c illustrates a case in which a 1.4 eV electron does not interact with the sphere and is instead deflected by the electric field. The percentage of deflected electrons that do not interact with  $\text{SiO}_2$  increases with total fluence because of the stronger electric fields that develop within the geometry (e.g., for  $n = 17$  in Fig. 2c,  $\sim 80\%$  of incident electrons are deflected, compared with 0% for  $n = 0$ ). In contrast, the higher-energy electron labeled 2 in Fig. 2c, with an energy of 53 eV, penetrates the sphere and implants at a depth of 1.2 nm.

### 3. Implementation

The simulation framework is designed for geometries filled with amorphous dielectric materials (e.g.,  $\text{SiO}_2$  spheres in vacuum). The charge-accumulation and electric-field calculations as-

sume that the deposited charge has no mobility. Instead, charge leakage from each voxel in  $O_{\text{field}}$  is treated macroscopically through the continuity equation for surface charge density (Eq. B.1 in Appendix B). This approximation is reasonable for dielectric materials with low electrical conductivities (e.g.,  $\vartheta \sim 10^{-13} \Omega^{-1} \text{m}^{-1}$ ). Additionally, the adopted physics list (Appendix A) is optimized for low-energy photons and electrons, typically below  $\sim 300 \text{ eV}$ , and for ions in the keV-range. Accurate tracking down to the nm-scale (as described in Section 2.2) provides a direct connection between microscopic ionization and scattering processes and macroscopic charge accumulation on grain surfaces.

### 3.1. Computational Resources

The simulations are performed on a high-performance computing cluster. Each iteration runs on a single node using 24 threads and requires at least 8 GB of memory per process, executed on a central processing unit. The computational load scales with the world size (shown in Fig. 1): the larger the world, the more octree boxes are generated and stored in memory. SLURM (Simple Linux Utility for Resource Management) is used as the workload scheduler and supports batch scripting. `g4chargeit` produces an executable in which iteration-specific commands are defined via macros and managed by Python scripts that automate the workflow. Jobs are submitted through SLURM such that each job begins after the previous one completes. The primary bottlenecks arise from inter-dependent threads, which limit parallelization efficiency, and from input/output read-write speeds associated with data handling.

### 3.2. Post-Processing of Results

The output files of our simulation tool include text files containing the electric field at each point of the adaptive octree and ROOT files containing particle trajectories within the geometry (see Appendix A of Ref. [38]). In Python, `pystyle` [39] is used to visualize the field maps, and `pyROOT` [40] is used to parse the ROOT files, which record all interactions experienced by each particle within the geometry. For example, the forces between neighboring grains can be calculated using both the field map and the processed ROOT data. The  $i$ -th component of the electric pressure, used as a measure of the force between grains, is given by

$$f_i = \sigma (\mathbf{E} \cdot \mathbf{n}) n_i, \quad (3)$$

where  $\sigma$  is the surface charge density and  $\mathbf{n}$  is the normal vector to the surface.

## 4. Verification

We specifically examine the charging of a group of grains within a regolith bed on the Moon. On the lunar dayside under quiet solar conditions, photons from the Sun strike the regolith at an incident angle of  $45^\circ$  and generate PEs when the incident photon energy exceeds the material work function. The PE current density is  $\sim 15$  times greater than the SW proton current density [26], causing PEs to dominate the charging dynamics. The SW is predominantly composed of 1 keV protons (incident at  $45^\circ$ ) and low-energy electrons (with energies of  $\sim 10 \text{ eV}$ , isotropic in angle) [12, 41]. Our approach enables replication of the stochastic nature of electron emission, reabsorption, and SW interactions on a grain-by-grain basis, offering a detailed granular perspective on the charging process while linking microscopic scattering processes to macroscopic charge accumulation and evolving electric fields. By incorporating the full range of charging

phenomena, the MC framework not only validates the core physics of the patched-charge model but also enables simulations of complex grain geometries—a capability absent in previous grain-scale models (e.g., Ref. [26]). Moreover, the direct modeling of photoemission and other ionization and scattering processes provides a comprehensive foundation for accurately simulating grain charging dynamics, which informs the subsequent discussion of charge accumulation in micro-cavities and its implications for grain lofting [42].

We provide quantitative benchmarking of `g4chargeit` against Ref. [26] and qualitative comparison with experimental results from Ref. [24]. The following subsections describe the geometry and simulation parameters used for verification. The grains in each geometric configuration are filled with  $\text{SiO}_2$  ( $\epsilon_r = 3.9$  [43], except  $\epsilon_r = 1$  for comparison with Ref. [26]) and placed in a galactic environment to model charging dynamics under realistic planetary conditions. Our MC approach inherits the validated cross-sections implemented in Geant4 [44, 45], making it highly versatile and enabling straightforward modification of material composition and grain geometry without altering the underlying physics models.

#### 4.1. Geometry for Benchmarking

We consider the following input geometry configurations:

*Regularly Packed Grains.* For the simplest configuration, we consider a hexagonally packed arrangement of spheres in the (010)-plane (cross-section in the  $xz$ -plane shown in Fig. 2). Each sphere has a radius of  $100\text{ }\mu\text{m}$  and is composed of  $\text{SiO}_2$  with a density of  $2.2\text{ g/cm}^3$ . We assume an amorphous and homogeneous  $\text{SiO}_2$  composition for simplicity; however, this can be readily modified in `g4chargeit` within the `DetectorConstruction` class using standard Geant4 commands [27]. The simulation volume is reduced to the smallest periodic unit surrounding the central sphere (Fig. 3a, pink box), and PBCs are enabled in the  $xy$ -plane to simulate an unbounded lateral repetition of grains. The stacking configuration and sphere radius are chosen to replicate the structure in Ref. [26], allowing for a quantitative comparison with our results.

*Irregularly Packed Grains.* We increase the geometric complexity by considering irregularly packed spherical grains (Fig. 3b) as an intermediate configuration between the regularly packed spheres and the realistic grain arrangement. Each sphere has a radius of  $25\text{ }\mu\text{m}$ , chosen to better represent the typical sizes of grains in lunar soil [47, 48]. We continue to assume a simple  $\text{SiO}_2$  composition but use a density of  $1.9\text{ g/cm}^3$ , reflecting measured densities of lunar simulants [24].

*Realistic Grain Configuration.* The grains are arranged in a realistic grain-stack configuration (Fig. 3c) that reproduces a geometry derived from synchrotron X-ray microtomography (Beamline 8.3.2, Advanced Light Source) of a planetary simulant. The isolated grains are arranged to fill a  $107 \times 121 \times 100\text{ }\mu\text{m}$  volumetric region to resemble regolith; the resulting porosity is  $\sim 52\%$ , in agreement with measured porosity values of lunar soil [47, 48]. This configuration also assumes a  $\text{SiO}_2$  composition with a density of  $1.9\text{ g/cm}^3$ .

#### 4.2. Incident Particle Distributions

We consider two distinct irradiation cases: (1) photon irradiation and (2) SW irradiation. Photons are sampled directly from the solar spectrum (Fig. 3d, Ref. [41]), with energies spanning between  $\sim 8\text{ eV}$  and  $\sim 350\text{ eV}$ , and uniformly strike the geometry at a  $45^\circ$  angle. The photoelectric effect is modeled stochastically (e.g., Fig. 2a). For the SW case, protons with energies of  $\sim 1\text{ keV}$  (red histogram in Fig. 3e, Ref. [46]) are incident at a  $45^\circ$  angle, while low-energy electrons are

incident isotropically. The SW electrons are sampled from the distribution shown in Fig. 3e (blue histogram, Ref. [46]), with an average energy of  $\sim 12.7$  eV and a current density five times that of the protons. The simulation parameters for each case and configuration are summarized in Table 1. The lunar equivalent time ( $t_M$ ) per iteration is calculated by scaling the number of emitted PE for photon irradiation and the number of protons striking the simulation volume for SW irradiation (i.e., particles at  $n = 0$  in Table 1) by the corresponding current densities on the Moon. We use average dayside current densities of  $4 \times 10^{-6}$  A/m<sup>2</sup> for emitted PEs,  $3 \times 10^{-7}$  A/m<sup>2</sup> for SW protons, and  $1.5 \times 10^{-6}$  A/m<sup>2</sup> for SW electrons [12, 26].

#### 4.3. Simulation Results

##### 4.3.1. Regularly Packed Grains

Figure 4 benchmarks our simulation against the analytical approach presented in Ref. [26]. Figure 4a shows the  $x$ -component of the electric field  $|E_x|$  for each iteration at a point  $37\ \mu\text{m}$  above the midpoint between the sphere centers (red point in Fig. 4b,c). The simulations are initialized at early times and iteratively advanced, allowing the electric field to evolve gradually until convergence with the analytical model (gray lines in Fig. 4). We find excellent agreement for both the photon and SW cases, which include modeling of the passive current density and charge dissipation (Eq. B.1). For the SW case, the simulations agree within  $\sim 4.85\%$ , indicating that g4chargeit accurately captures charge accumulation in this simple geometry and reliably reproduces the temporal evolution of the electric field under the same irradiation conditions as in Ref. [26].

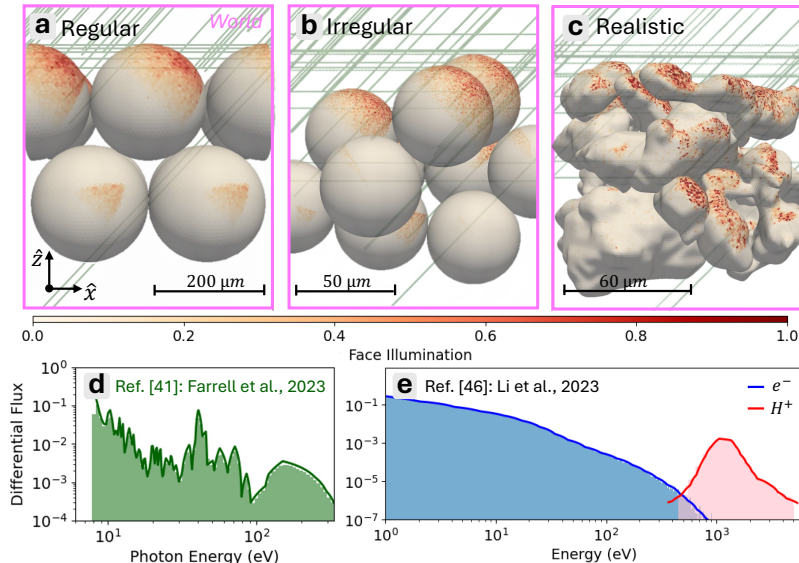


Figure 3: Face illumination of (a) regularly packed grains, (b) irregularly packed grains, and (c) a realistic grain configuration. Particle trajectories of photons incident at  $45^\circ$  are shown in green. The horizontal green lines are due to PBC in the  $x$ -direction, where particles re-enter the box after exiting through the sides. (d) Photon energies are sampled from the differential flux at solar minimum (Ref. [41]). (e) Particles from the SW plasma are sampled from the differential flux of electrons (blue) and protons (red) (Ref. [46]). SW electrons are isotropic with an average energy of  $\sim 12.7$  eV, and SW protons are incident at  $45^\circ$  angle with an average energy of  $\sim 1.2$  keV.

However, for photon irradiation, our simulation results cannot be directly compared with those of Ref. [26]. The photoelectric effect is not explicitly calculated in Ref. [26]; instead, PEs with an average energy of 1 eV are isotropically emitted from the illuminated faces. This assumption produces a population of low-energy electrons whose trajectories are readily perturbed by the strong electric fields that develop between the grains, ultimately contributing to the nonlinear growth and eventual saturation of the electric field (top gray line in Fig. 4a). In our simulations, photons are sampled directly from the solar spectrum (Fig. 3d), and the photoelectric effect is modeled explicitly (e.g., Fig. 2a), removing the need to impose assumptions about the secondary yield and instead utilizing the validated cross-sections implemented in Geant4 [44, 45]. Because the energy of PEs is  $E_\gamma - \phi$ , where  $\phi$  is the work function ( $\sim 8$  eV), the generated PEs can have energies as high as  $\sim 340$  eV, significantly larger than the 1 eV PE population in Ref. [26]. These more energetic PEs require stronger electric fields to deflect them, which, in turn, leads to an increased  $E_x$  at saturation in our results (extrapolated region, orange dashed line in Fig. 4a). As a result, the electric field is expected to plateau at  $8.4 \times 10^5$  V/m at  $t_M = 120$  s, when the charge dissipation term starts to dominate the surface charge variation (Eq. B.1). This value is  $\sim 2 \times$  larger than that reported in Ref. [26] of  $|E_x| = 3.6 \times 10^5$  V/m at  $t_M = 120$  s, but remains within the expected range for a constant conductivity of  $\vartheta \sim 10^{-13} \Omega^{-1} m^{-1}$ . Nevertheless, our simulation results are in close agreement with Ref. [26] (Fig. 4a).

The attractive or repulsive force between neighboring spherical grains is quantified using the electric pressure (Eq. 3). The  $x$ -component of the electric pressure is shown in Fig. 4d,e, where adjacent regions of opposing sign (red–blue) correspond to an attractive interaction. For the regularly packed spherical grains, we find that the grains experience a net attractive force, consistent with Ref. [26]. However, both our simulations and the grain-scale model in Ref. [26] stand in conflict with experimental observations, which instead report a repulsive force inside micro-cavities that may contribute to grain lofting [25, 42, 23]. This discrepancy suggests that regularly packed spheres may not capture key physical effects responsible for the experimentally observed repulsion. The patched-charge model has previously explored the importance of micro-cavities using both experimental and numerical approaches [24, 25, 23]. Although it represents an improvement over the conventional uniform shared-charge assumption, it still relies on simplifications—most notably idealized grain shapes and the neglect of transient charge fluctuations and stochastic electron trajectories—that may limit its applicability under more realistic

Table 1: Lunar equivalent time ( $t_M$ ) for each configuration (regularly packed, irregularly packed, and realistic packing) is calculated using average dayside current densities of  $4 \times 10^{-6}$  A/m<sup>2</sup> for emitted PEs and  $3 \times 10^{-7}$  A/m<sup>2</sup> for SW protons [26]. Specifically,  $t_M$  is obtained by normalizing the number of particles incident on the simulation volume by the area of the illumination plane and the corresponding average dayside current density.

Illumination Plane ( $\mu\text{m}$ )	Regularly Packed		Irregularly Packed		Realistic	
	$\gamma$	SW	$\gamma$	SW	$\gamma$	SW
Incident particles per $n$	1,000,000	80,000	500,000	10,000	300,000	10,000
Fluence per $n$ ( $\mu\text{m}^{-2}$ )	8.33	0.67	39.68	0.79	23.21	0.77
	PE	$\text{H}^+$	PE	$\text{H}^+$	PE	$\text{H}^+$
Particles at $n = 0$	8,446	13,060	3,270	1,235	2,917	1,409
$t_M$ per $n$ (ms)	2.82	58.12	10.40	52.35	9.04	58.23

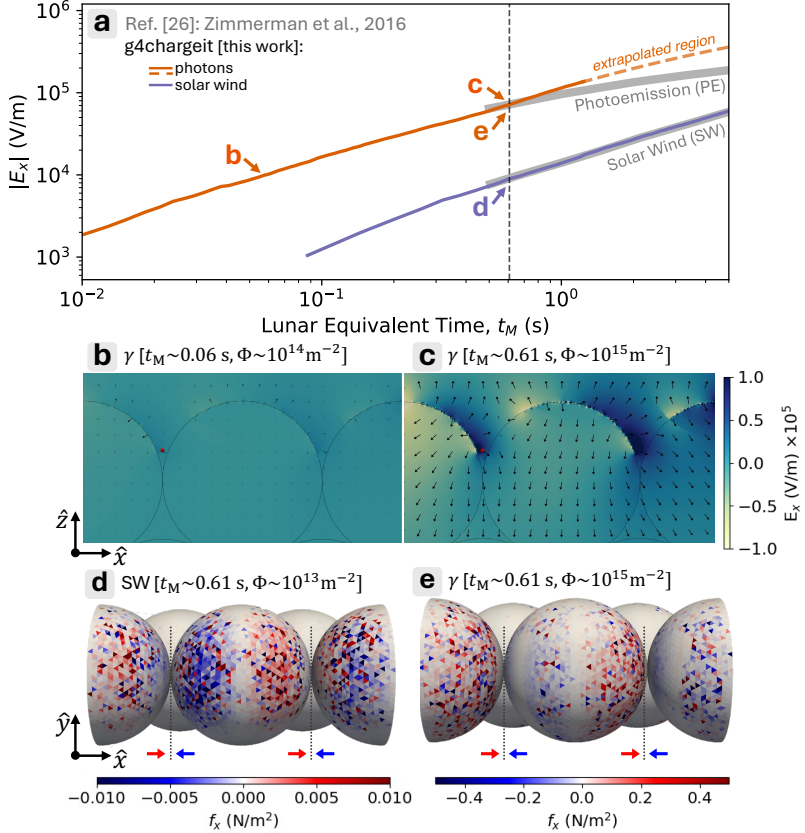


Figure 4: (a)  $|E_x|$  plotted against the equivalent lunar time  $t_M$  for the photon (orange) and SW (purple) cases at the point  $37\mu\text{m}$  above the midpoint between the sphere centers; red point in (b) and (c). The photon results are extrapolated using the expected extension (dashed orange line, least-squares fit to Eq. B.1). Results from Ref. [26] are overlaid for comparison (gray lines). (b,c) Interpolated electric-field vectors in the  $xz$ -plane at (b)  $t_M \sim 0.06$  s and (c)  $t_M \sim 0.61$  s. The background color shows the  $x$ -component of the electric field  $E_x$ . (d,e) Electric pressure ( $x$ -component) at  $t_M \sim 0.61$  s for (d) SW irradiation (equivalent fluence of  $\Phi \sim 10^{13} \text{ m}^{-2}$ ) and (e) photons irradiation (equivalent fluence of  $\Phi \sim 10^{15} \text{ m}^{-2}$ ). An attractive force between the spheres is observed for both SW and photon irradiation (adjacent regions with opposite colors, i.e., red-blue).

conditions. To investigate whether geometric complexity, such as micro-cavities, can produce the repulsive regions observed in experiments, we apply our self-consistent MC framework to simulate charge accumulation in irregularly packed grains.

#### 4.3.2. Irregularly Packed Grains

Figure 5 illustrates charge accumulation on irregularly packed spherical grains for photon (Fig. 5a,b) and SW (Fig. 5c,d) irradiation. The  $z$ -component of the electric pressure  $f_z$  is shown on the surface of each sphere, while the background color represents the  $x$ -component of the electric field  $E_x$ , and the vectors indicate the electric field in the  $xz$ -plane (scaled by the field magnitude). These results address the question posed earlier: can repulsive forces emerge within micro-cavities for different grain packings? In contrast to the attractive forces observed for regu-

larly packed grains (Fig. 4d,e), the irregular configuration exhibits distinct repulsive regions (i.e., red-red or blue-blue in Fig. 5b,d). As the system evolves, charged particles are scattered into micro-cavities (black-outlined regions in Fig. 5b,d), generating electrostatic repulsion between neighboring grains. This repulsion is particularly evident for the SW case (Fig. 5d), where substantial charge buildup within the cavity produces forces that can eventually push the spheres apart. At an equivalent time for photon irradiation (Fig. 5b), the repulsive force is weaker due to the lower electric-field strength within the cavity. We find that the irregular packing can induce repulsive forces between spherical grains, whereas regular hexagonal packing (Fig. 4d,e) produces symmetric pressure patterns that induce attraction. The repulsive force observed within the micro-cavity in Fig. 5 qualitatively agrees with Ref. [24], in which the authors found that exposure to charged particles generates electrostatic repulsion, while exposure to photons alone does not produce comparable field strengths within micro-cavities.

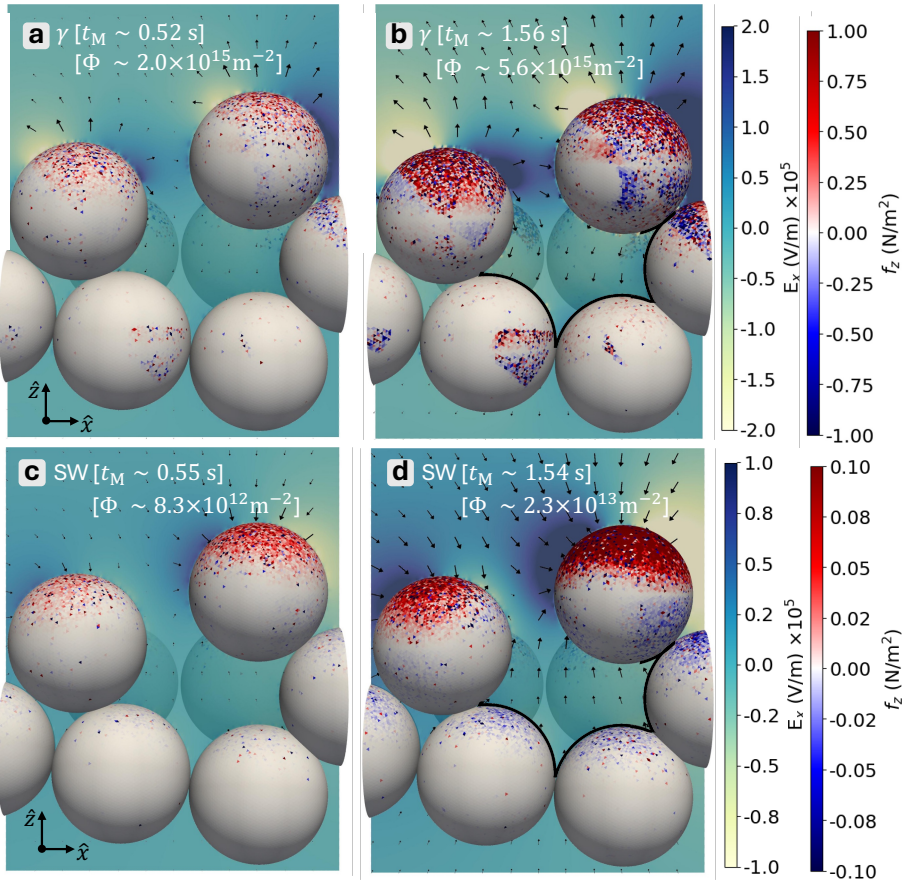


Figure 5: Simulation results for irregularly packed grains under photon irradiation at (a)  $t_M \sim 0.52$  s (corresponding fluence  $\Phi \sim 2.0 \times 10^{15} \text{ m}^{-2}$ ) and (b)  $t_M \sim 1.56$  s ( $\Phi \sim 5.6 \times 10^{15} \text{ m}^{-2}$ ), followed by the SW case of (c)  $t_M \sim 0.55$  s ( $\Phi \sim 8.3 \times 10^{12} \text{ m}^{-2}$ ) and (d)  $t_M \sim 1.54$  s ( $\Phi \sim 2.3 \times 10^{13} \text{ m}^{-2}$ ). Each panel shows the  $x$ -component of the electric field ( $E_x$ , yellow-blue colormap), the  $z$ -component of the electric pressure ( $f_z$ , seismic colormap), and the electric-field vector (black arrows) in the  $xz$ -plane.

It is important to consider the timescales over which our simulations are valid, since the spheres remain static during the time-discretized MC runs. Consequently, this framework cannot be used directly to simulate grain lofting; instead, it captures the precursor electric fields that develop within micro-cavities before the forces become large enough to move the spheres. In Fig. 5d,  $f_z$  reaches a maximum of  $\sim 0.1 \text{ N/m}^2$  within a micro-cavity, corresponding to a force of  $F_c \sim 10^{-13} \text{ N}$ . The force due to lunar gravity on a silica sphere of  $50 \mu\text{m}$  diameter is  $F_g = 2.0 \times 10^{-10} \text{ N}$ , implying that  $F_c$  would need to increase by roughly three orders of magnitude before lofting could occur. Therefore, on the timescales of seconds,  $F_c \ll F_g$ , and the simulations shown in Fig. 5 remain well within the regime in which the assumption of static geometry is valid. Additionally, the magnitude of the forces obtained in our simulations is consistent with both experimental observations of lofting, occurring at electron fluences of  $\sim 10^{17} \text{ e}^-/\text{m}^2$  [42], and estimates of electrostatic repulsion in micro-cavities from the patched-charge model,  $F_c \sim 10^{-10} \text{ N}$  [25], which are three to four orders of magnitude larger than the values shown in Fig. 5.

#### 4.3.3. Realistic Grain Configuration

Figure 6 shows the time evolution of the  $x$ -component of the electric pressure  $f_x$  for the realistic grain configuration, in which charge accumulation within micro-cavity is observed by comparing Fig. 6a with Fig. 6b for photon irradiation and Fig. 6c with Fig. 6d for SW irradiation. Figure 6b,d present snapshots of the surface charge distribution at later times, including zoomed-in insets of representative micro-cavities at  $t_M \sim 1.56 \text{ s}$  and  $5.10 \text{ s}$  for photon and SW irradiation, respectively. Interpreting the electrostatic force is challenging for such a complex geometry, as it depends on the local face normal (Eq. 3); however, a qualitative understanding of the forces shown in the insets of Fig. 6b,d can be obtained by considering  $f_x$  in the context of the coordinate axes. Because adjacent regions in the insets of Fig. 6b,d have the same sign (i.e., blue-blue or red-red), neighboring grains experience repulsive interactions, which could increase the porosity of the grain stacking if the system were evolved to longer times. Nevertheless, the observed charge accumulation within micro-cavities is consistent with the patched-charge model [25], in which the emission and reabsorption of charged particles generate large surface charge densities and resulting repulsive forces within grain micro-cavities.

Charge accumulation in realistic geometries produces a markedly more complex distribution than in spherical grains. Broken symmetries and sharp morphological features introduce micro-cavities that generate localized regions of shearing, cohesion, and strong repulsion, none of which are macroscopically uniform. As irradiation progresses, the heterogeneous electric-pressure patterns can promote dielectric breakdown and increase the likelihood of grain lofting due to strong electric fields that concentrate along protrusions and recessed regions of the grains. The lack of symmetry helps explain the repulsion seen in realistic geometries in Fig. 6b,d. It leads to a highly nonuniform electric-pressure patterns that fail to form the opposing pressure-pair structures observed in regularly packed spherical grains, resulting instead in localized repulsion dictated by grain geometry. Because our simulation framework is built on Geant4, the open-source code `g4chargeit` can be readily adapted to study other charging phenomena within lunar science and the broader planetary science community.

## 5. Other Applications

The core implementation of `g4chargeit` functions as a general-purpose KMC tool for studying the charging of dielectric materials. It is readily adaptable to airless planetary bodies through

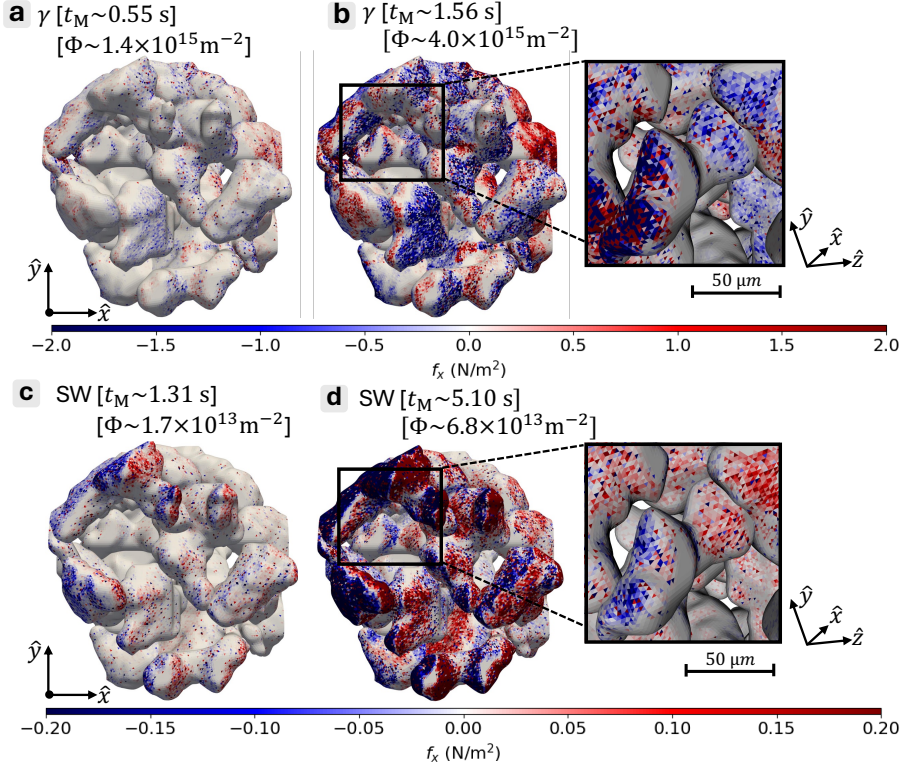


Figure 6: Electric pressure ( $x$ -component) for the realistic packing of grains under photon irradiation at (a)  $t_M \sim 0.55$  s (corresponding fluence  $\Phi \sim 1.4 \times 10^{15} \text{ m}^{-2}$ ) and (b)  $t_M \sim 1.56$  s ( $\Phi \sim 4.0 \times 10^{15} \text{ m}^{-2}$ ), with the inset showing the electric pressure within a micro-cavity. The analogous results for SW irradiation are shown at (c)  $t_M \sim 1.31$  s ( $\Phi \sim 1.7 \times 10^{13} \text{ m}^{-2}$ ) and (d)  $t_M \sim 5.10$  s ( $\Phi \sim 6.8 \times 10^{13} \text{ m}^{-2}$ ). The zoomed-in insets in (b) and (d) show the generation of a repulsive force (adjacent regions of the same color, i.e., blue-blue or red-red) for both irradiation scenarios.

modifications of the grain geometry, material composition, and incident particle distributions.

*Advantage of the Geant4 Monte Carlo Approach.* The Geant4 MC framework offers distinct advantages over deterministic field solvers for modeling electrostatic charging of dielectric materials in complex planetary environments. The accumulation of discrete charged particles naturally resolves local charge inhomogeneities, enabling the calculation of spatially varying electric pressure by connecting the microscopic, atomic-scale interactions to the micron-scale charge inhomogeneities. Unlike analytical multipole models, this particle-based approach inherently accounts for higher-order moments, which are critical for accurately modeling short-range interactions between irregular grains. In addition, the framework supports arbitrary geometries and materials without modification of the underlying physics models. This flexibility is achieved by leveraging validated Geant4 cross-sections to model complex scattering processes such as secondary electron emission and backscattering. At the same time, this approach can be computationally intensive and becomes inefficient at length scales where continuum approximations are valid. The strength of the Geant4 framework lies in bridging atomistic interaction physics and macroscopic charge evolution while incorporating the complexities of real materials.

*Applications within Planetary Science.* Within the planetary science community, g4chargeit can be used to quantify how the geometry of realistic grains influences charge accumulation and to assess the role of these parameters in the eventual electrostatic lofting of grains. For example, soil porosity, grain size, and material composition can be systematically modified to study their effects on charge accumulation (e.g., comparison with Ref. [42]). Beyond grain structure and composition, the properties of the incident particle population can also be adjusted to investigate additional charging processes relevant to the Moon and other airless bodies. For instance, solar energetic particles can be modeled; because these particles penetrate deeper into the material and undergo more complex scattering, g4chargeit leverages the Geant4 architecture to stochastically simulate the associated ionization and scattering processes. In such cases, deeper energy deposition makes dielectric screening increasingly important. These examples illustrate the connection that our code establishes between microscopic scattering interactions and macroscopic charge accumulation and electric-field evolution (e.g., Ref. [49]).

*Potential Utility beyond Space Science.* Additional applications include simulating dust mitigation technologies such as electrostatic dust shields, placing limits on dielectric breakdown in materials, modeling spacecraft charging in the presence of external electric or gravitational fields, and extending Geant4’s capabilities for condensed-matter and semiconductor device simulations [50]. More broadly, the framework is applicable to diverse domains, including photovoltaic devices and electrostatic processes in biological systems such as DNA.

## 6. Concluding Remarks

In this work, we present a KMC approach to model the time evolution of electrostatic charging on dielectric materials. We apply our code, g4chargeit, to simulate the charging of non-spherical dust grains within a lunar regolith bed, a harsh electrostatic environment in which charged dust can significantly influence local plasma conditions, dust transport, and adhesion. By leveraging a MC approach, inherited from Geant4, we model the generation of secondary electrons and the associated electric fields on non-spherical dielectric grains, developing a generalizable and adaptable framework. We show that charge accumulation leads to localized enhancements in surface charge density, resulting in electric-field heterogeneities that strongly influence subsequent particle interactions, secondary emission, and ultimately grain-scale dynamics. By explicitly resolving secondary electron production and time-dependent charge accumulation, the model naturally captures microscopic charging processes that connect to macroscopic behavior. We demonstrate that this multiscale simulation approach can handle complex, heterogeneous regolith structures and provide a versatile code with applications beyond planetary science.

### Credit authorship contribution statement

**Kush P. Gandhi:** Preparation of original draft, Conceptualization, Methodology, Validation. **Advik D. Vira:** Preparation of revised draft, Formal Analysis, Supervision. **William M. Farrell:** Manuscript review, Conceptualization, Validation. **Nikolai Simonov:** Methodology. **Alvaro Romero-Calvo:** Manuscript review, Methodology, Validation. **Thomas M. Orlando:** Manuscript review, Funding acquisition, Project administration. **Phillip N. First:** Manuscript review, Methodology, Funding acquisition. **Zhigang Jiang:** Manuscript review, Conceptualization, Supervision, Funding acquisition.

## Declaration of Competing Interest

The authors declare that they have no known competing financial interests or personal relationships that could have appeared to influence the work reported in this paper.

## Acknowledgments

The authors thank Dr. Makoto Asai for numerous conversations regarding the development of our simulation framework and Romain Fonteyne for his invaluable assistance in advancing the early stages of this work. This research was supported by the NASA Solar System Exploration Research Virtual Institute (SSERVI), under cooperative agreement number NNH22ZDA020C (CLEVER, Grant number: 80NSSC23M022). It was also supported in part through research cyber infrastructure resources and services provided by the Partnership for an Advanced Computing Environment (PACE) at the Georgia Institute of Technology, Atlanta, Georgia, USA.

## Appendix A. Modification to Geant4 Factory Physics Lists

The radiation transport physics is managed using the factory physics list FTFP\_BERT\_EMX, which we modify by replacing the standard electrostatic (EM) physics package with G4EmStandardPhysics\_option4. This option employs the low-energy Livermore models to compute interaction cross-sections using evaluated databases, including EPDL97 (Evaluated Photon Data Library) [51], EPICS2017 (Evaluated Photon Data Library), EEDL (Evaluated Electron Data Library) [52], EADL (Evaluated Atomic Data Library) [53], and electron binding energies derived from Scofield’s data [54]. These databases, combined with experimental measurements and theoretical models, allow Geant4 to calculate total and sub-shell-resolved photoelectric cross-sections, Compton scattering cross-sections, secondary-particle energy spectra, electron binding energies, and transition probabilities for fluorescence and Auger emission.

To accurately model low-energy particles, we further configure the EM processes via G4EmParameters. Atomic de-excitation processes—including fluorescence, Auger electron production and cascades, and Particle-Induced X-ray Emission (PIXE)—are enabled, along with the Continuous Slowing Down Approach (CSDA) to model continuous energy loss. The default production thresholds are reduced to permit energy deposition down to a few eV for electrons and 10 eV for hadrons. The stopping range of ions and electrons from Geant4 is validated against Stopping and Range of Ions in Matter (SRIM) [55, 56] and CASINO [57], respectively. Together with the low-energy Livermore model, these physics choices enable accurate modeling of the low-energy charge generation and transport processes characteristic of SW irradiation. Each emission, absorption, and scattering event is treated probabilistically and self-consistently based on the local energy spectrum and electromagnetic environment, allowing the simulation to resolve transient charge fluctuations and spatial heterogeneities within regolith micro-cavities.

## Appendix B. Incorporation of Charge Dissipation

While the Geant4 framework accounts for the stochastic deposition of charge from incident currents, it does not inherently model the subsequent charge relaxation, or dissipation, through

the dielectric regolith. The net temporal change in surface charge density,  $\dot{\sigma}$ , is governed by the continuity equation, given as [26]:

$$\dot{\sigma} = j \exp(-\frac{\sigma}{\Sigma}) - \frac{\vartheta}{\epsilon_r \epsilon_0} \sigma, \quad (\text{B.1})$$

where the first term represents the net charging current (e.g., from PE, secondary emission, SW flux), and the second term is the ohmic dissipation term, which must be incorporated explicitly to model charge transport within the material. For lunar regolith, the temperature-dependent electrical conductivity,  $\vartheta(T)$ , is [58]:

$$\vartheta(T) = 6 \times 10^{-18} \exp(0.0230T) \Omega^{-1} \text{m}^{-1}. \quad (\text{B.2})$$

To implement the charge dissipation, we first calculate the net surface charge density  $\sigma$  within each voxel of the field octree  $O_{\text{field}}$ , and then apply the dissipation term as an adjustment to the net charge in the voxel over the iteration time step. The updated charge distribution is subsequently saved to the master charge list for the next simulation iteration ( $n + 1$ ). A constant electrical conductivity of  $\vartheta \sim 10^{-13} \Omega^{-1} \text{m}^{-1}$  (corresponding to an equivalent temperature of 425 K) is used for all results presented in this paper. Over a simulation time of 10 s, the induced temperature changes based on local charge accumulation are negligible ( $< 2 \text{ K}$ ); therefore, the time dependence of the dissipation term can be neglected. However, this effect can be incorporated for systems in which temperature variations relative to the ambient thermal bath are significant.

## References

- [1] M. Casalegno, G. Raos, R. Po, Methodological assessment of kinetic monte carlo simulations of organic photovoltaic devices: The treatment of electrostatic interactions, *The Journal of Chemical Physics* 132 (9) (2010) 094705. [arXiv:https://pubs.aip.org/aip/jcp/article-pdf/doi/10.1063/1.3337909/15876736/094705\\_1\\_online.pdf](https://pubs.aip.org/aip/jcp/article-pdf/doi/10.1063/1.3337909/15876736/094705_1_online.pdf), doi:10.1063/1.3337909.
- [2] L. Guldbrand, L. G. Nilsson, L. Nordenskiöld, A monte carlo simulation study of electrostatic forces between hexagonally packed dna double helices, *The Journal of Chemical Physics* 85 (11) (1986) 6686–6698. [arXiv:https://pubs.aip.org/aip/jcp/article-pdf/85/11/6686/18962003/6686\\_1\\_online.pdf](https://pubs.aip.org/aip/jcp/article-pdf/85/11/6686/18962003/6686_1_online.pdf), doi:10.1063/1.451450.
- [3] T. Sun, V. Minhas, N. Korolev, A. Mirzoev, A. P. Lyubartsev, L. Nordenskiöld, Bottom-up coarse-grained modeling of dna, *Frontiers in Molecular Biosciences* Volume 8 - 2021 (2021). doi:10.3389/fmolb.2021.645527.
- [4] T. Wang, K. Hess, G. J. Iafrate, Time-dependent ensemble monte carlo simulation for planar-doped gaas structures, *Journal of Applied Physics* 58 (2) (1985) 857–861. doi:10.1063/1.336155.

[5] A. Akturk, N. Goldsman, G. Pennington, Self-consistent ensemble monte carlo simulations show terahertz oscillations in single-walled carbon nanotubes, *Journal of Applied Physics* 102 (7) (2007) 073720. doi:10.1063/1.2794690.

[6] X. Q. Yu, C. HongFei, Z. QiuGang, W. JianZhao, S. WeiHong, Z. Hong, Z. JiQing, Z. WeiYing, C. Zhe, S. SiPei, J. XiangHong, Leakage current of grounded dielectrics in electron radiation as a diagnostic method to evaluate the deep charging hazards in space, *IEEE Transactions on Nuclear Science* 63 (2) (2016) 1306–1313. doi:10.1109/TNS.2016.2537839.

[7] J. Wang, R. Liu, R. Xiao, A. Ping, J. Liu, M. Zhang, Q. Li, Optimized design of slip ring assembly for aerospace to reduce deep dielectric charging, *IEEE Transactions on Nuclear Science* 69 (4) (2022) 915–924. doi:10.1109/TNS.2022.3157670.

[8] K. Fichthorn, W. Weinberg, Theoretical foundations of dynamical monte carlo simulations, *The Journal of chemical physics* 95 (2) (1991) 1090–1096. doi:10.1063/1.461138.

[9] J. Wu, Y. Zhi, X. Dang, P. Wang, B. Zhang, Weak conductive channel effect of glass fabric on deep charging of polyimide in geo, *IEEE Transactions on Nuclear Science* 72 (2) (2025) 164–174. doi:10.1109/TNS.2024.3519769.

[10] T. Ramachandran, A. Ali, F. A. Deader, H. Shafeekali, L. Zheng, H. Butt, M. Rezeq, Dual influence of size and electric field on gold nanoparticles: Insights into 2d monolayer assembly, *Langmuir* 41 (2) (2025) 1271–1280, pMID: 39772803. doi:10.1021/acs.langmuir.4c03580.

[11] C. M. Katzen, D. J. Brinker, R. Kress, The effects of lunar dust accumulation on the performance of photovoltaic arrays (1991).

[12] R. F. Willis, M. Anderegg, B. Feuerbacher, B. Fitton, *Photoemission and Secondary Electron Emission from Lunar Surface Material*, Springer Netherlands, Dordrecht, 1973.

[13] S. Hazra, V. Réville, B. Perri, A. Strugarek, A. S. Brun, E. Buchlin, Modeling solar wind variations over an 11 year cycle with alfvén wave dissipation: A parameter study, *The Astrophysical Journal* 910 (2) (2021) 90. doi:10.3847/1538-4357/abe12e.

[14] S. Popel, L. Zelenyi, A. Golub', A. Dubinskii, Lunar dust and dusty plasmas: Recent developments, advances, and unsolved problems, *Planetary and Space Science* 156 (2018) 71–84, dust, Atmosphere, and Plasma Environment of the Moon and Small Bodies. doi:10.1016/j.pss.2018.02.010.

[15] R. Goodwin, *Apollo 17: The NASA Mission Reports*, vol. 1 (2002).

[16] J. R. Gaier, *The Effects of Lunar Dust on EVA Systems During the Apollo Missions*, Tech. rep., National Aeronautics and Space Administration (2007).

[17] J. E. Colwell, S. Batiste, M. Horányi, S. Robertson, S. Sture, Lunar surface: Dust dynamics and regolith mechanics, *Reviews of Geophysics* 45 (2) (2007). doi:10.1029/2005RG000184.

[18] R. Christoffersen, J. F. Lindsay, S. K. Noble, M. A. Meador, J. J. Kosmo, J. A. Lawrence, L. Brostoff, A. Young, T. McCue, Lunar Dust Effects on Spacesuit Systems: Insights from the Apollo Spacesuits, Tech. rep., National Aeronautics and Space Administration (2008).

[19] A. Romero-Calvo, J. Hammerl, H. Schaub, Touchless potential sensing of differentially charged spacecraft using secondary electrons, *Journal of Spacecraft and Rockets* 59 (5) (2022) 1623–1633. doi:10.2514/1.A35355.

[20] A. Romero-Calvo, K. Champion, H. Schaub, Enabling ultraviolet lasers for touchless spacecraft potential sensing, *IEEE Transactions on Plasma Science* 51 (9) (2023) 2468–2481. doi:10.1109/TPS.2023.3264914.

[21] T. M. Flanagan, J. Goree, Dust release from surfaces exposed to plasma, *Physics of Plasmas* 13 (12) (2006) 123504. doi:10.1063/1.2401155.

[22] T. E. Sheridan, A. Hayes, Charge fluctuations for particles on a surface exposed to plasma, *Applied Physics Letters* 98 (9) (2011) 091501. doi:10.1063/1.3560302.

[23] Z. Wang, D. Tian, Z. Ma, C. Zhao, Y. Liu, Y. Liu, Y. Ding, Z. Shen, An electrostatic lofting model based on adhesion separation characteristics for lunar dust, *Planetary and Space Science* 184 (2020) 104883. doi:10.1016/j.pss.2020.104883.

[24] X. Wang, J. Schwan, H.-W. Hsu, E. Grün, M. Horányi, Dust charging and transport on airless planetary bodies, *Geophysical Research Letters* 43 (12) (2016) 6103 – 6110. doi:10.1002/2016GL069491.

[25] X. Wang, J. Schwan, N. Hood, H.-W. Hsu, E. Grün, M. Horányi, Experimental Methods of Dust Charging and Mobilization on Surfaces with Exposure to Ultraviolet Radiation or Plasmas, *Journal of Visualized Experiments* 134 (2018) 57072. doi:10.3791/57072.

[26] M. I. Zimmerman, W. M. Farrell, C. M. Hartzell, X. Wang, M. Horanyi, D. M. Hurley, K. Hibbitts, Grain-scale supercharging and breakdown on airless regoliths, *Journal of Geophysical Research: Planets* 121 (10) (2016) 2150–2165. doi:<https://doi.org/10.1002/2016JE005049>.

[27] S. Agostinelli, J. Allison, K. Amako, J. Apostolakis, H. Araujo, P. Arce, M. Asai, D. Axen, S. Banerjee, G. Barrand, F. Behner, L. Bellagamba, J. Boudreau, et al., Geant4—a simulation toolkit, *Nuclear Instruments and Methods in Physics Research Section A: Accelerators, Spectrometers, Detectors and Associated Equipment* 506 (3) (2003) 250–303. doi:10.1016/S0168-9002(03)01368-8.

[28] J. Allison, K. Amako, J. Apostolakis, H. Araujo, P. Arce Dubois, M. Asai, G. Barrand, R. Capra, S. Chauvie, R. Chytracek, G. Cirrone, G. Cooperman, et al., Geant4 developments and applications, *IEEE Transactions on Nuclear Science* 53 (1) (2006) 270–278. doi:10.1109/TNS.2006.869826.

[29] J. Allison, K. Amako, J. Apostolakis, P. Arce, M. Asai, T. Aso, E. Bagli, A. Bagulya, S. Banerjee, G. Barrand, B. Beck, A. Bogdanov, D. Brandt, et al., Recent developments in geant4, *Nuclear Instruments and Methods in Physics Research Section A: Accelerators, Spectrometers, Detectors and Associated Equipment* 835 (2016) 186–225. doi:10.1016/j.nima.2016.06.125.

[30] R. Chytracek, J. McCormick, W. Pokorski, G. Santin, Geometry description markup language for physics simulation and analysis applications, *IEEE Transactions on Nuclear Science* 53 (5) (2006) 2892 – 2896, cited by: 131. doi:10.1109/TNS.2006.881062.

[31] L. Dagum, R. Menon, Openmp: An industry-standard api for shared-memory programming, *IEEE Comput. Sci. Eng.* 5 (1) (1998) 46–55. doi:10.1109/99.660313.

[32] R. Brun, F. Rademakers, Root — an object oriented data analysis framework, *Nuclear Instruments and Methods in Physics Research Section A: Accelerators, Spectrometers, Detectors and Associated Equipment* 389 (1) (1997) 81–86, new Computing Techniques in Physics Research V. doi:https://doi.org/10.1016/S0168-9002(97)00048-X.

[33] D. Meagher, Geometric modeling using octree encoding, *Computer Graphics and Image Processing* 19 (2) (1982) 129–147. doi:https://doi.org/10.1016/0146-664X(82)90104-6.

[34] Z. Gan, Z. Xu, Efficient implementation of the barnes-hut octree algorithm for monte carlo simulations of charged systems, *Science China Mathematics* 57 (7) (2014) 1331–1340.

[35] R. S. Martin, J.-L. Cambier, Octree particle management for DSMC and PIC simulations, *Journal of Computational Physics* 327 (2016) 943–966. doi:10.1016/j.jcp.2016.01.020.

[36] J. R. Dormand, P. J. Prince, A family of embedded runge–kutta formulae, *Journal of Computational and Applied Mathematics* 6 (1980) 19–26.

[37] W. M. Farrell, D. M. Hurley, V. J. Esposito, J. L. McLain, M. I. Zimmerman, The statistical mechanics of solar wind hydroxylation at the Moon, within lunar magnetic anomalies, and at Phobos, *Journal of Geophysical Research: Planets* 122 (1) (2017) 269–289. doi:10.1002/2016JE005168.

[38] A. D. Vira, E. M. Mone, E. A. Ryan, P. T. Connolly, K. Smith, C. D. Roecker, K. E. Mesick, T. M. Orlando, Z. Jiang, P. N. First, Designing a boron nitride polyethylene composite for shielding neutrons, *APL Materials* 11 (10) (2023) 101104. arXiv:https://pubs.aip.org/aip/apm/article-pdf/doi/10.1063/5.0163377/18147885/101104\_1\_5.0163377.pdf, doi:10.1063/5.0163377.

[39] C. B. Sullivan, A. A. Kaszynski, Pyvista: 3d plotting and mesh analysis through a streamlined interface for the visualization toolkit (vtk), *Journal of Open Source Software* 4 (37) (2019) 1450. doi:10.21105/joss.01450.

[40] Galli, Massimiliano, Tejedor, Enric, Wunsch, Stefan, A new pyroot: Modern, interoperable and more pythonic, *EPJ Web Conf.* 245 (2020) 06004. doi:10.1051/epjconf/202024506004.

[41] W. M. Farrell, J. S. Halekas, M. Horányi, R. M. Killen, C. Grava, J. R. Szalay, M. Benna, P. E. Clark, M. R. Collier, A. Colaprete, J. Deca, R. C. Elphic, S. Fatemi, Y. Futaana, M. Holmström, D. M. Hurley, G. Y. Kramer, P. R. Mahaffy, M. N. Nishino, S. K. Noble, Y. Saito, A. R. Poppe, K. D. Rutherford, X. Wang, S. Yokota, The Dust, Atmosphere, and Plasma at the Moon, *Reviews in Mineralogy and Geochemistry* 89 (1) (2023) 563–609, \_eprint: <https://pubs.geoscienceworld.org/msa/rimg/article-pdf/89/1/563/6072927/rmg.2023.89.13.pdf>. doi:10.2138/rmg.2023.89.13.

[42] N. Hood, A. Carroll, R. Mike, X. Wang, J. Schwan, H. Hsu, M. Horányi, Laboratory Investigation of Rate of Electrostatic Dust Lofting Over Time on Airless Planetary Bodies, *Geophysical Research Letters* 45 (24) (Dec. 2018). doi:10.1029/2018GL080527.

[43] G. R. Olhoeft, D. W. Strangway, Dielectric properties of the first 100 meters of the Moon, *Earth and Planetary Science Letters* 24 (3) (1975) 394–404. doi:10.1016/0012-821X(75)90146-6.

[44] Z. Li, C. Michelet, S. Incerti, V. Ivanchenko, M. Novak, S. Guatelli, H. Seznec, Implementation of the epics2017 database for photons in geant4, *Physica Medica* 95 (2022) 94–115. doi:<https://doi.org/10.1016/j.ejmp.2022.01.008>.

[45] A. Albqoor, E. Ababneh, S. Okoor, I. Zahran, Validation of electromagnetic physics models and electron range in geant4 brachytherapy application, *Nuclear Engineering and Technology* 55 (1) (2023) 229–237. doi:<https://doi.org/10.1016/j.net.2022.09.018>.

[46] S. Li, A. R. Poppe, T. M. Orlando, B. M. Jones, O. J. Tucker, W. M. Farrell, A. R. Hendrix, Formation of lunar surface water associated with high-energy electrons in Earth’s magnetotail, *Nature Astronomy* 7 (12) (2023) 1427–1435. doi:10.1038/s41550-023-02081-y.

[47] W. D. Carrier, Lunar soil grain size distribution, *The Moon* 6 (3–4) (1973) 250–263. doi:10.1007/BF00562206.

[48] J. Goguen, A. Sharits, A. Chiaramonti, T. Lafarge, E. Garboczi, Three-dimensional characterization of particle size, shape, and internal porosity for Apollo 11 and Apollo 14 lunar regolith and JSC-1A lunar regolith soil simulant, *Icarus* 420 (2024) 116166.

doi:<https://doi.org/10.1016/j.icarus.2024.116166>.

- [49] J. S. Halekas, G. T. Delory, R. P. Lin, T. J. Stubbs, W. M. Farrell, Lunar surface charging during solar energetic particle events: Measurement and prediction, *Journal of Geophysical Research: Space Physics* 114 (A5) (2009). arXiv:<https://agupubs.onlinelibrary.wiley.com/doi/pdf/10.1029/2009JA014113>, doi:<https://doi.org/10.1029/2009JA014113>.
- [50] M. Kelsey, R. Agnese, Y. Alam, I. A. Langroudy, E. Azadbakht, D. Brandt, R. Bunker, B. Cabrera, Y.-Y. Chang, H. Coombes, R. Cormier, M. Diamond, E. Edwards, E. Figueroa-Feliciano, J. Gao, P. Harrington, Z. Hong, M. Hui, N. Kurinsky, R. Lawrence, B. Loer, M. Masten, E. Michaud, E. Michelin, J. Miller, V. Novati, N. Oblath, J. Orrell, W. Perry, P. Redl, T. Reynolds, T. Saab, B. Sadoulet, K. Serniak, J. Singh, Z. Speaks, C. Stanford, J. Stevens, J. Strube, D. Toback, J. Ullom, B. VanDevender, M. Vissers, M. Wilson, J. Wilson, B. Zatschler, S. Zatschler, G4cmp: Condensed matter physics simulation using the geant4 toolkit, *Nuclear Instruments and Methods in Physics Research Section A: Accelerators, Spectrometers, Detectors and Associated Equipment* 1055 (2023) 168473. doi:<https://doi.org/10.1016/j.nima.2023.168473>.
- [51] D. E. Cullen, J. H. Hubbell, L. Kissel, Epdl97: the evaluated photo data library '97 version, Tech. rep., Lawrence Livermore National Lab., CA (United States) (09 1997). doi:[10.2172/295438](https://doi.org/10.2172/295438).
- [52] S. Perkins, D. Cullen, S. Seltzer, Tables and graphs of electron-interaction cross sections from 10 ev to 100 gev derived from the llnl evaluated electron data library (eedl), z = 1 to 100, Unknown -1 (10 1991). doi:[10.2172/5691165](https://doi.org/10.2172/5691165).
- [53] S. T. Perkins, D. E. Cullen, M. H. Chen, J. Rathkopf, J. Scofield, J. H. Hubbell, Tables and graphs of atomic subshell and relaxation data derived from the llnl evaluated atomic data library (eadl), z = 1–100, Tech. rep., Lawrence Livermore National Lab., CA (United States) (10 1991). doi:[10.2172/10121422](https://doi.org/10.2172/10121422).
- [54] J. H. SCOFIELD, 6 - radiative transitions, in: B. CRASEMANN (Ed.), *Atomic Inner-Shell Processes*, Academic Press, 1975, pp. 265–292. doi:<https://doi.org/10.1016/B978-0-12-196901-1.50012-1>.
- [55] J. F. Ziegler, J. P. Biersack, *The Stopping and Range of Ions in Matter*, Springer-Verlag US, 1985. doi:[10.1007/978-1-4615-8103-1\\_3](https://doi.org/10.1007/978-1-4615-8103-1_3).
- [56] J. Ziegler, *The Stopping and Ranges of Ions in Matter*, Pergamon, 2013.
- [57] D. Drouin, P. Hovington, R. Gauvin, Casino: A new monte carlo code in c language for electron beam interactions—part ii: Tabulated values of the mott cross section, *Scanning* 19 (1) (1997) 20–28. doi:<https://doi.org/10.1002/sca.4950190103>.

[58] R. J. L. Grard (Ed.), Photon and particle interactions with surfaces in space, Vol. 37 of Astrophysics and Space Science Library, 1973. doi:10.1007/978-94-010-2647-5.